

Regular Paper

Novel Processing Tools for Automated Doppler Picture Velocimetry (DPV) evaluation

Seiler, F.*¹, Pichler, A.*¹, Pfaff, R.*² and Srulijes, J.*¹

*1 French-German Research Institute of Saint-Louis (ISL)
5, rue du Général Cassagnou, 68301 Saint-Louis, France

*2 Control Theory and Application Centre, Coventry University,
Priory Street, Coventry, Great Britain

Received 1 October 2008
Revised 18 May 2009

Abstract : A unique technique, the Doppler Picture Velocimetry (DPV), for measuring and visualizing velocities especially in hypersonic gas flows is presented. By means of a Michelson interferometer (MI) the Doppler shifted light scattered by tracers is transformed into an image showing Fizeau fringes. The image fringe distribution provides information on the Doppler frequency shift which is related to the velocity of the particles crossing a light sheet plane. To overcome former disadvantages of DPV, the optical set-up as well as the processing scheme have been improved significantly. Two schemes have been tested in recent times for fringe processing: 1) an alternative process, the Least Square Estimators (LES) and 2) an algorithm based on a technique using Fast Fourier Transformations (FFT) to examine the DPV images in the frequency domain. The new DPV algorithms now allow an automated calculation of the velocity profiles from the Doppler pictures without manual fringe tracing as it had to be done in the past. Both methods are compared by means of Mach 6 flows around a wedge and a sphere produced in the ISL high energy shock tunnel STA. TiO₂ particles are illuminated by a laser light sheet which was perpendicularly arranged to the main flow direction. Light observation via the MI from the side (90° to illumination) informs on the vertically oriented velocity through the DPV images.

Keywords : 2D Doppler velocity measurements, hypersonic flow, light sheet, tracer, velocity visualization, Michelson interferometer, sphere and wedge flow velocity visualization

1. History of global velocimetry

Several laser-based techniques have been developed worldwide for measuring the flow velocity distribution in a light sheet, i.e. in a plane, crossing a gas flow. A well-established technique is Particle Image Velocimetry (PIV), which relies on the statistical analysis of geometrical particle displacements (Merzkirch, 1990). Doppler Global Velocimetry (DGV) analyses the Doppler frequency shift of light scattered by tracer particles by an amplitude light filter (Meyers, 1992). The Doppler frequency can also be analyzed by a special wide-field Michelson interferometer (MI) designed at ISL by Oertel et al., 1982. This method, called Doppler Picture Velocimetry (DPV), was further developed by Seiler et al., 1987. Several disadvantages, concerning particularly the optical set-up of the MI, have already been improved as described in Seiler et al., 2002. The DPV version (Seiler et al., 2004) uses two pictures, which are taken simultaneously: a Doppler picture showing

the frequency shift of the light scattered by the moving tracer particles and a reference picture with no frequency shift. In the paper of Seiler et al., 2004, a simple and straightforward user manipulated DPV picture processing algorithm is described and applied for evaluating the velocity picture published. Further enhancement of the Doppler picture processing tools was performed by Pfaff et al., 2005 in using interactive processing software, based on the Java Advanced Imaging Bibliotheca. By mouse click the user marks, point by point, the center of the dark MI fringe lines. These points are linearly interpolated and stored in a $n \times m$ matrix, which size is similar to that of the CCD chip of the camera used, as reported by Seiler et al., 2006. The drawings, especially the pseudo color images, were prepared with the Matlab software and the Matlab Image Processing Toolbox (see The MathWorks, 2005).

Newly, Pichler et al., 2007 and Pfaff et al., 2007 developed new automated DPV image processing software, using: 1) a FFT based algorithm (Fast Fourier Transformation) and 2) by using Least Squares Estimators (LES). These techniques are described and compared to each other in order to show the advantages and disadvantages of both algorithms for DPV picture processing.

2. The Doppler Picture Velocimeter

2.1 Optical set-up

The global DPV technique for the measurement of a velocity field in two dimensions in a gas flow is based on the observation of light reflected by tracer particles seeded in the flow. The flow is illuminated with monochromatic coherent light by a laser and the resulting Doppler shift of the reflected light is visualized by use of a Michelson interferometer (MI). This interferometer makes it possible to measure Doppler frequency shifts in the range of 10^{-5} of the original frequency for Mach 6 flows by transforming it into fringe shifts in the Fizeau fringe pattern, on which the MI is adjusted.

The DPV technique uses a unique MI, as described in principle by Seiler et al., 2006, see Fig. 1. The laser light with frequency ν_L is divided into two parts by a splitter cube with a 30%-to-70% light intensity ratio. The 30% part is focused onto two dispersion plates in plane Σ . Nowadays, the use of two plates compared to only one (see Pichler et al., 2007), greatly reduces unwanted speckle noise in the reference image. The 70%-part illuminates the measurement plane, also called Σ , which crosses the gas flow as a light sheet. In order to visualize the velocity distribution, TiO_2 tracer particles are seeded and the light scattered from these particles is focused into the specially designed MI, which is used here as a wide field interferometer. In the same way, the light coming from the dispersion plates, as reference light, is also directed into the MI as depicted in Fig. 1. The “reference” light bundle is colored in blue and the “Doppler picture” light bundle in yellow. Both parts are perpendicularly polarized to each other by the polarizing beam splitter T1. Entering the MI the “reference” and the “Doppler picture” light (highlighted in green), pass geometrically the same ways but are completely independent from each other due to its different polarizations.

The MI in Fig.1 consists of the beam splitter cube T2, the two mirrors M_1 and M_2 and the glass block G between M_2 and T2. The scattered light coming from the object planes Σ , the tracer scattered light as well as the reference light, is divided by the second beam splitter T2 into two parts of equal intensity, which were focused on mirror M_1 (leg 1) and on mirror M_2 (leg 2). With the lenses used, the image of the planes Σ (dispersion plates and tracers) on M_1 and M_2 is transferred via the polarizing beam splitter T3 to the image planes Σ' , forming the Doppler picture on the CCD1 camera and the reference picture on CCD2. The light passing the two interferometer legs 1 and 2 is able to form a two beam interference pattern in the image planes Σ' . As a result of that interference the light intensity I at all image points P' in Σ' , on the CCD1 as well as on the CCD2 camera chip, depends on the phase difference $\Delta\varphi$ originated in the two legs as given in the following (\hat{I} : max. intensity) with :

$$I = \hat{I} \cos^2 \frac{\Delta\varphi}{2} . \quad (1)$$

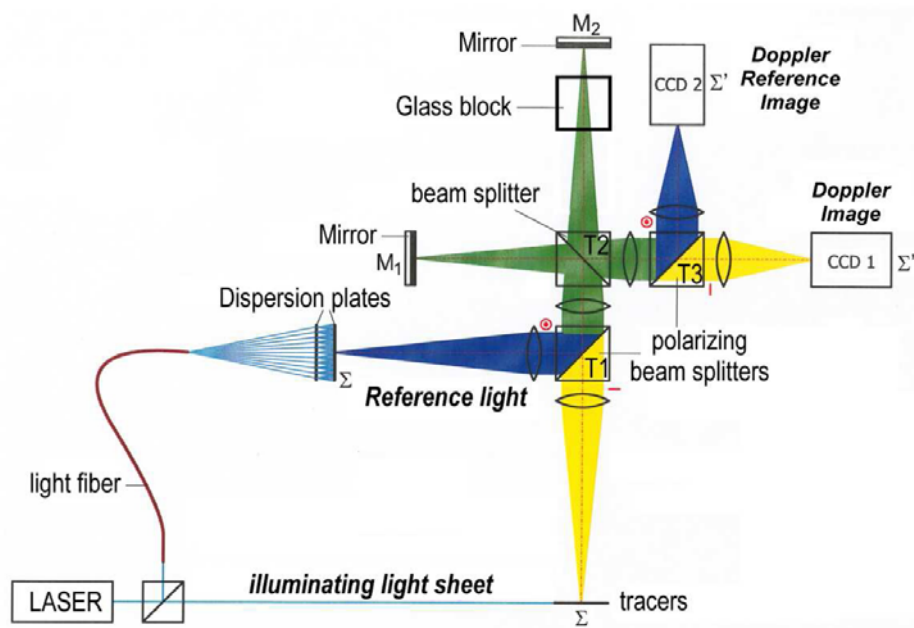


Fig. 1. Optical set-up of the Michelson interferometer

The phase difference $\Delta\varphi$ is a function of the optical path difference $\Delta\phi$, as given by Seiler et al., 2006:

$$\frac{\Delta\varphi}{2\pi} = \nu \frac{\Delta\phi}{c_0} . \quad (2)$$

The optical path difference is defined as

$$\Delta\phi = 2n|\ell_2 - \ell_1| . \quad (3)$$

In differentiating equation (2) with regard to $d\nu$, the result is:

$$d\left(\frac{\Delta\varphi}{2\pi}\right) = \frac{\Delta\phi}{\lambda_0} \frac{d\nu}{\nu} . \quad (4)$$

The light scattered from the light sheet plane Σ is, in the case of moving tracer particles, Doppler shifted from frequency ν_R (R: laser reference) to ν_D (D: detector, i.e. the MI). The frequency change of the scattered light, as seen by the MI,

$$d\nu = \nu_D - \nu_R , \quad (5)$$

is transformed into a change $d(\Delta\varphi)$, see equation (4), of the phase difference $\Delta\varphi$ between the two legs of the Michelson interferometer. The $d(\Delta\varphi)$ change causes at each pixel of the CCD cameras variations

$$dI = -d(\Delta\varphi) \frac{\hat{I}}{2} \sin \Delta\varphi \quad (6)$$

of the interference light intensity illuminating the planes Σ' compared with the initially adjusted reference light intensity distribution. This dI -change ($dI = I_D - I_R$) informs on the $d(\Delta\varphi)$ -shift and by

relation (4) on the frequency shift $d\nu$, which is proportional to the tracer speed. The initially adjusted intensity distribution I_R and the Doppler shifted distribution I_D are represented by

- (I_R): the reference picture light intensity which is formed by the light coming from the dispersion plates and passing the MI without being frequency shifted (blue coloured light path in Fig.1) and
- (I_D): the Doppler picture light intensity created by the light scattered by tracer particles crossing the light sheet (yellow coloured light path in Fig.1).

Both pictures, the reference and the Doppler picture, are taken simultaneously as described in Pichler et al., 2007, replacing the former DPV version (Seiler et al., 2002), in which both pictures could only be taken one after the other.

2.2 Tuning

The MI is adjusted to interference fringes by turning the mirror M_1 by a very small angle β to produce a linear changing optical path difference $\Delta\phi$ along M_1 . The amount of fringes which appear in the image planes Σ' depend on the turning angle β . As an example, the reference fringe system is depicted in Figs. 8 (LES in section 5) and 12 (FFT in section 6) for the DPV experiments performed with a wedge in a high-speed Mach-6-flow.

In high-speed flows small tracer particles have to be seeded in order to follow velocity changes in shock waves with the smallest delay as possible. For this study TiO_2 tracer particles with a diameter of about $1\ \mu\text{m}$ have been used, as mentioned in the chapter 2.1. As the MI is tuned to interference fringes, its appearance is independent from the particle density. The absolute particle density is not extremely important for DPV purposes. The only condition is that the CCD cameras used for capturing the scattered light get enough light energy for taking and storing the interference fringe patterns.

3. The shock tube equipment

3.1 Shock tunnel STA

Nowadays the high energy shock tubes at ISL are employed as hypersonic wind tunnels. A view of both shock tunnel facilities is shown in Fig. 2. This laboratory picture shows in the foreground the driven tubes and in the background the measuring sections in front of the dump tanks. Shock tube STA on the left hand and shock tube STB on the right hand one. The shock tube itself is divided into the high-pressure driver tube and the low-pressure driven tube, see Fig. 3.

In the driver tube a preferably light driver gas is compressed up to 450 bar. At a determined driver gas pressure the steel membrane dividing the high and low-pressure parts bursts. In this moment, a compression shock runs through the driven tube where nitrogen is contained under a pressure of up to 5 bar. At the same time, an expansion wave runs in the opposite direction and is reflected from the left end of the driver tube. The compression shock propels the gas in the driven tube in front of the entry of the Laval nozzle where it is compressed and heated and remains for a short time almost stationary. The driven gas then expands through the Laval nozzle resulting in a quasi-stationary hypersonic flow into the measurement chamber. The resulting measurement time ranges from 1 up to 4 ms, depending on the flow conditions. Tests covered in this work were performed at Mach number 6 and at a static pressure of $8 \pm 0.5\ \text{kPa}$ and a temperature of about 220 K, resembling the conditions in the atmosphere at an altitude of 17.5 km. For this nozzle conditions a measurement time of about 2 ms is achieved.



Fig. 2. Shock Tube Laboratory at ISL

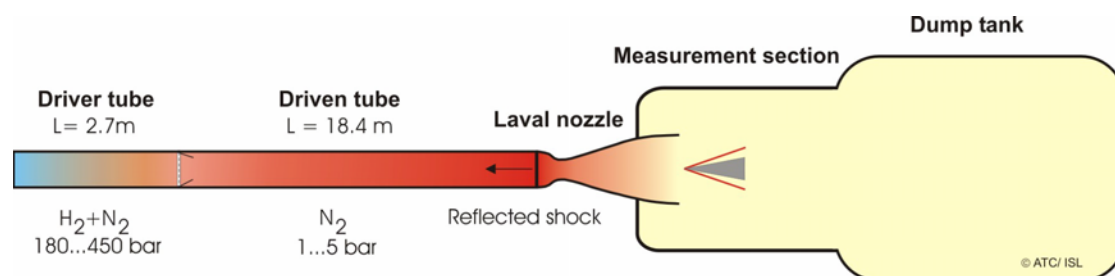


Fig. 3. Principle sketch of shock tunnel STA of ISL

3.2 Arrangement of optics

The Mach-6-nozzle used in shock-tunnel STA is placed at the end of the driven tube and blows into the measurement section, mounted in front of the dump tank. Through two windows each side and one at the top of the measurement section, an optical access for flow illumination and flow observation is achieved. The photo montage in Fig. 4 shows the illuminating optics, a laser light sheet hitting the wedge from above, and the observation of the scattered light via the MI from the side. The light sheet is produced by a laser (vector \vec{L} in Fig. 5) which illuminates a plane axially oriented in the middle of the wedge flow. The observation by means of the MI was done from the side in the direction of vector \vec{R} . The wedge flow is quasi two-dimensional, with flow vectors \vec{u} (horizontal orientation) and \vec{v} (vertical orientation, see Fig. 5). With this optical set-up, the projection of the velocity component \vec{v} in the bisector of the angle formed by the illumination and observation directions is measured.

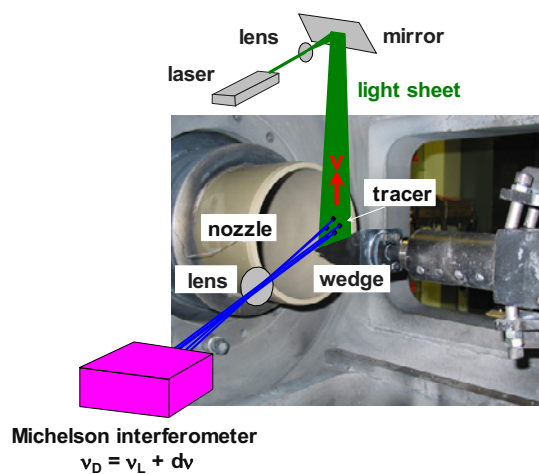
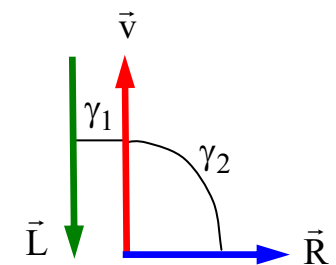


Fig. 4. DPV picture visualization

Fig. 5. Vectors \vec{L} , \vec{R} and \vec{v}

4. Automated picture processing algorithms

4.1 Development goals

The aim of the work described in this paper concerns the development of automated processing software for the evaluation of the fringe images produced by the DPV method. Although many software tools for PIV and DGV are available, the existing procedures are not suitable to process the DPV pictures taken with the optical MI set-up given in Fig. 1. The Doppler images are interferometric fringe images with a determined structure, in the present case a \cos^2 -shaped system of fringes, which is distorted by mainly two sources of noise, i.e., the particle distribution and the digital camera used. While the particle distribution disturbs the light intensity distribution in the Doppler images, the camera introduces the so-called readout noise and the image sensor noise. The readout noise is caused in the conversion process from CCD registers to grey values in analogue to digital converters, amplifiers and charge to voltage converters. It is commonly assumed to be Gaussian white noise. Further noise sources are present in form of lenses, beam splitters and polarizing screens in the optical set-up. These noise sources can be neglected due to their comparably small influence. The noise source can thus be assumed to be additive white noise with exception of the particle distribution noise, which is a low-frequency component. But nevertheless, the accuracy of the velocity distribution from DPV pictures is only small influenced by these sources of noise as explained by Pfaff, 2007 and Pichler and George, 2007.

4.2 Tools applied

The DPV picture analysis methods developed in the past, e. g. Seiler et al. ,2002, 2004, see also section 1, require manual or interactive fringe tracing by the operator and are quite time consuming. For that reason, Pfaff et al., 2007, Pfaff et al., 2007 and Pichler et al., 2007 developed new automated DPV image processing software without need of fringe tracing. The scheme of Pichler et al., 2007 uses a FFT-based algorithm (Fast Fourier Transformation) to examine the Doppler images in the frequency domain while Pfaff's method, 2007 is focused on the application of the Least Squares Estimators (LES), both described in the next sections.

5. LES model

5.1 Fringe description

The luminance in each pixel (x, y) of the reference and the Doppler pictures is, see relation (1):

$$I(x, y) = \hat{I} \cos^2 \frac{\Delta\varphi(x, y) + \omega y}{2}. \quad (7)$$

The fringe distribution is periodical and the additional term ωy corresponds to the fringe frequency, introduced by tilting one of the mirrors. In equations (7-9), the \hat{I} is the maximal possible light intensity; see equation (1), too.

5.2 Image model

The image model is determined by the fringe structure given above and the additional components, where the cylindrical and spherical lenses are predominant. These lenses introduce a varying luminance according to one dimensional and two dimensional Gaussian curves, respectively. By denoting the reference image with I_R and the Doppler image with I_D , both images can be written as

$$I_D(x, y) = \hat{I} \exp\left(\frac{-(x - \mu^2)}{2\sigma^2}\right) \cos^2\left(\frac{\Delta\varphi(x, y) + \omega y}{2}\right). \quad (8)$$

where μ and σ are values given by the tuning of the optical MI-set-up and they can be chosen by adjusting the lenses.

$$I_R(x, y) = \hat{I} \exp\left(\frac{-(x - \mu^2) - (y - \mu)^2}{2\sigma^2}\right) \cos^2\left(\frac{\omega y}{2}\right). \quad (9)$$

Since mean and standard deviation as well as phase shift occur nonlinearly in these equations, they are not suitable for parameter estimation as intended. Further influence on the luminance distribution is the particle distribution in the flow, which cannot be guaranteed to be uniform and can be modeled as multiplicative Gaussian noise. Considering these influences in the model will lead to too many degrees of freedom in the model, therefore a simplification followed by linearization is necessary. This process is applied for the DPV pictures, the reference and the Doppler pictures, in almost the same way and is described in the following section.

5.3 Simplifications

By assuming the local maximum light intensity to be a slowly varying parameter, it is possible to omit the luminance distribution caused by the optical components and the particle distribution. The maximum local light intensity is denoted as

$$I_0(x, y) = \hat{I} \exp\left(\frac{-(x - \mu^2)}{2\sigma^2}\right) \varepsilon_d, \quad (10)$$

where ε_d is the particle density noise. The fringe system can be linearized to allow estimation of the parameters and may be written as:

$$I(x, y) = \frac{1}{2} I_0 \sin \Delta\varphi(x, y) \cos \omega y - \frac{1}{2} I_0 \cos \Delta\varphi(x, y) \sin \omega y + \frac{1}{2} I_0, \quad (11a)$$

with

$$I(x, y) = \alpha(x, y) \cos \omega y - \beta(x, y) \sin \omega y + \gamma(x, y). \quad (11b)$$

In this way, it is possible to express the phase variation as

$$\Delta\varphi(x,y)=\arctan_2\left(\frac{\beta(x,y)}{\alpha(x,y)}\right), \quad (12)$$

where \arctan_2 denotes the four-quadrant inverse tan-function. This phase variation is proportional to the velocity in the pixel under consideration, thus the problem of measuring the velocity distribution is reduced to the estimation of parameters present linearly in an appropriate formulation of the image model. One hyper parameter is contained nonlinearly in equations (11a, b), which corresponds to the fringe frequency. This frequency is estimated separately from α , β and γ by using convolution and peak-picking, therefore the parameters can be estimated with linear optimisation techniques.

5.4 Estimators

As suitable estimators, online estimators, namely Recursive Least Squares Estimators and a Kalman Filter, were considered. In order to limit the number of estimator candidates a simulation study was led. In this study, a simulated image column with a typical light intensity variation and a step change in phase was processed with various estimators. The image data was processed column-wise as well, since no meaningful metric for considering neighboring pixels in addition to the actual pixel was found. In Fig. 6, the simulated image column is given in comparison to the estimated values of different estimators, namely a RLS estimator with fixed forgetting factor $\lambda = 0.98$ (RLS ff), a RLS estimator with covariance reset (RLS CR) triggered on prediction error of more than 20% and additionally a Kalman filter (KF).

The estimators are compared according to the mentioned interferogram simulations, for details see Pfaff, 2007. This resulted in a list of advantages and drawbacks for each single estimator and helped to choose the appropriate one for the evaluation of the experimental images. A simulation is obviously helpful for this purpose, since all parameters are known and can be compared easily. The numerical experiment conducted for this purpose can be considered as one column of a DPV Doppler image, at a typical resolution of 1000 pixel per column. In this numerical calculation the shock was seen almost as a step change to the gas velocity. This step is extended over 10 pixels due to the inertia of the tracer particles.

For the comparison of least squares estimators applied to a simulated image column, it is convenient to state a quantitative measure of performance, which together with the more qualitative analysis given by Pfaff, 2007 may help to choose the right estimator for this purpose. Therefore the Euler norm of the error in light intensity ei_k and the error in the phase shift $e\varphi_k$ was calculated and given in Table 1. From this table it can be seen that with respect to the error in the phase shift $e\varphi_k$, the ‘‘RLS ff’’ as well as the ‘‘RLS CR’’ and the ‘‘KF’’ perform reasonably well and all three may be considered a good choice for the DPV evaluation gaining the phase change $d(\Delta\varphi)$ for Doppler frequency change evaluation, dependence see equation (4). From these considerations the velocity precision is approximated to the order of plus/minus some 10 m/s.

Table 1. Phase and intensity error comparisons

	RLS ff.	RLS CR	KF
$e\varphi_2$	8.52	6.02	8.40
ei_2	16.40	7.54	6.92

All estimators (RLS ff and RLS CR) are able to well track the image column, but only the Kalman filter and the RLS with covariance reset follow the step change well (Fig. 7), which qualifies them as estimators for the images. However, in application to the real Doppler images, the

RLS with fixed forgetting performed better: Thus, the best image estimator, the RLS estimator with fixed forgetting factor (ff) was chosen for DPV picture processing.

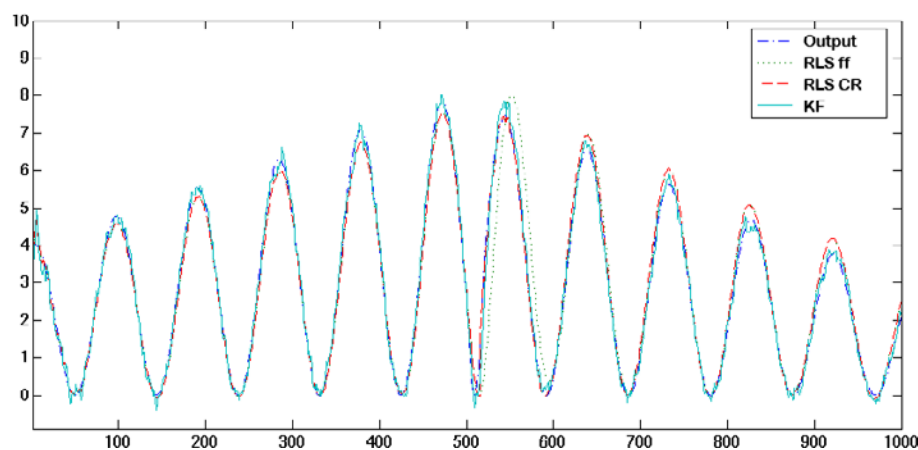


Fig. 6. Simulated image column

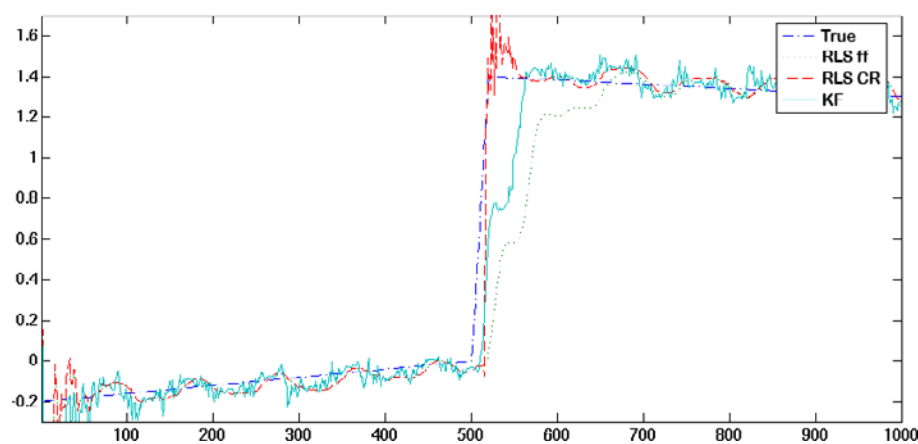


Fig. 7. True and estimated phases of different estimators

5.5 LES velocity results

5.5.1 Wedge flow

In Fig. 8, the Doppler and reference image pair for a wedge in Mach-6-flow is shown. For flow illumination an Ar⁺-laser was used and the CCD exposure time was 2 ms. The upward processed velocity component is given in Fig. 9 in pseudo color representation. This image shows strong artifacts along the line of the shock, the estimator converges to the true velocity value too slowly at these locations. It is assumed that this is due to the absolute error measurement in the RLS estimator. This lets the output prediction error appear lower in dark image areas, while the phase prediction error is high. Due to these artifacts clearly visible in Fig. 9, the velocity estimation is not reasonable in the space in-between shock and wedge surface towards the tip of the wedge surface. Therefore about 25% of the total wedge length, as shown in Fig. 15, was not treated by the LES-algorithm in the wedge's front region and hence was suppressed in Fig. 9.

For the processing of the Doppler image a RLS with fixed forgetting factor $\lambda = 0.95$ and covariance reset, triggered on the line of the oblique shock, was used. The reference image was processed using an RLS with fixed forgetting factor $\lambda = 0.995$, no covariance reset was applied.

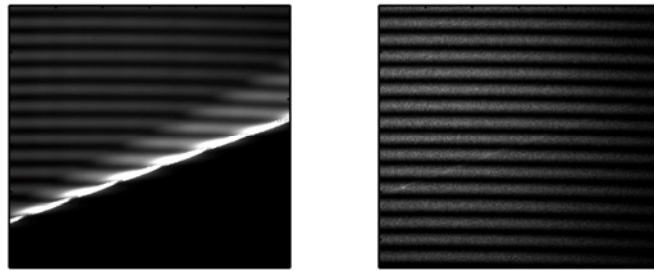


Fig. 8. Doppler and reference image for the wedge

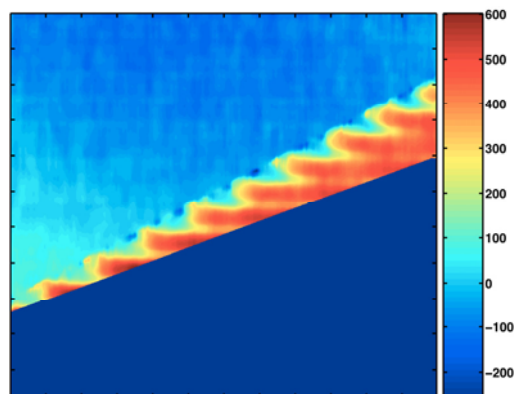


Fig. 9. LES processed upward velocity component of flow above a wedge in Mach-6-flow

5.5.2 Sphere flow

Moreover, the velocity distribution around a sphere in horizontal Mach-6-flow is measured. Here as well, the pressure conditions resemble a flight at an altitude of approximately 17.5 km, as already mentioned in section 3. The Doppler and reference image pair is given in Fig. 10, a pseudo color representation of the upward velocity field in Fig. 11. The RLS parameters use a fixed forgetting factor of $\lambda = 0.97$ for the Doppler image and $\lambda = 0.995$ for the reference image.



Fig. 10. Doppler and reference image for the sphere

5.5.3 Remarks

Based on the preliminary studies presented herein on LES it was possible to successfully estimate the velocities around two elementary bodies, the sphere and the wedge. The continuously varying velocity field around the sphere was processed well and the velocity estimation gave reasonable results. In the case of the wedge, the velocity image exhibited some artifacts that may be explained by the way the estimator handles the prediction error. This prediction error is measured absolutely, which in the case of a sinusoidal fringe system leads to relatively large errors that do not correct the next estimate accordingly. Some methods may be considered to cope with these artifacts and may form the basis for further research. These are the adaptation of the estimators presented here

to measure the prediction error relatively, the introduction of a suitable vector norm instead of the scalar cost function and the investigation of suitable transformations such as the unscented transform.

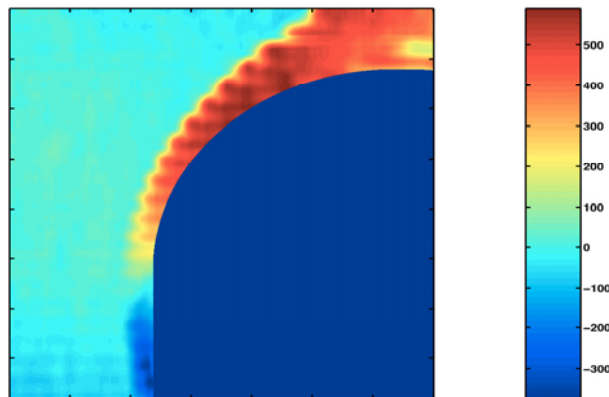


Fig. 11. LES processed upward velocity component of flow around a sphere in Mach-6-flow

6. FFT method

6.1 Necessities

In order to measure the fringe displacements automatically with the FFT-based technique (Fast Fourier Transformations), the Doppler pictures must fulfill the following requirements:

1. The maximum fringe shift (measured in pixels) should not exceed half of the distance between the minima of two fringes, the fringe spacing. So the glass block used in the MI has to be adapted to the expected velocity range.
2. Reference and Doppler images need to be matched in size and rotation. Marker images should be taken before the experiment.

6.2 Image filtering

The captured Doppler images contain the velocity variation information in form of fringe displacements. The original reference and Doppler images, taken by the MI, are given in Fig. 12 with the fringe arrangement obviously present in both pictures. In the flow in front of the oblique shock produced over the wedge surface the vertical velocity is zero, i.e. there the initially tuned fringe pattern is present as it is in the reference sample. By the oblique shock, the flow turns upwards and the fringes are shifted as seen in the Doppler picture in Fig. 12. The Doppler images are filtered first to facilitate the automated detection of fringe shifts by the computer. All unwanted brightness variations (not belonging to the fringe system) and high-frequency background noise are removed from the pictures while preserving the original fringe displacements in all details. Fig. 13 shows the filtered reference and Doppler pictures for the flow over the wedge from Figure 12.

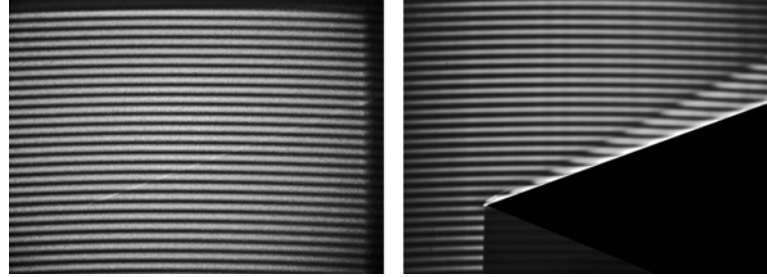


Fig. 12. Original reference and Doppler pictures

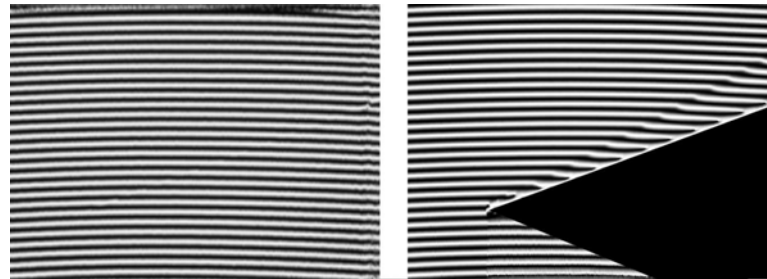


Fig. 13. Filtered reference and Doppler pictures

6.3 Velocity profile calculation

The filtered images are processed by an automated DPV algorithm. Additionally, two black/white mask images are needed, one masking out non-analyzable areas (e.g. saturations, no tracers) and one image masking out the model contour to show its placement in the shock-tunnel and its dimensions. Equation (13) describes the brightness information of each pixel of the filtered Doppler image as:

$$g(x, y) = c(x, y)e^{j2\pi f_0 y} + c^*(x, y)e^{-j2\pi f_0 y}. \quad (13)$$

A value of $g(x, y) = -1$ corresponds to the brightness minimum, a value of $g(x, y) = 1$ to the maximum. The parameter $j = \sqrt{-1}$. The phase shift can be found in $\alpha(x, y)$ or its complex conjugate $c^*(x, y)$:

$$c(x, y) = \frac{1}{2} b(x, y) e^{j\Delta\phi(x, y)}. \quad (14)$$

To extract the phase shift information from (14), each column of the Doppler image is transformed in the frequency domain using the FFT (Example column of a typical Doppler image is seen in Fig. 14):

$$G(f, x) = C(f - f_0, x) + C^*(f - f_0, x). \quad (15)$$

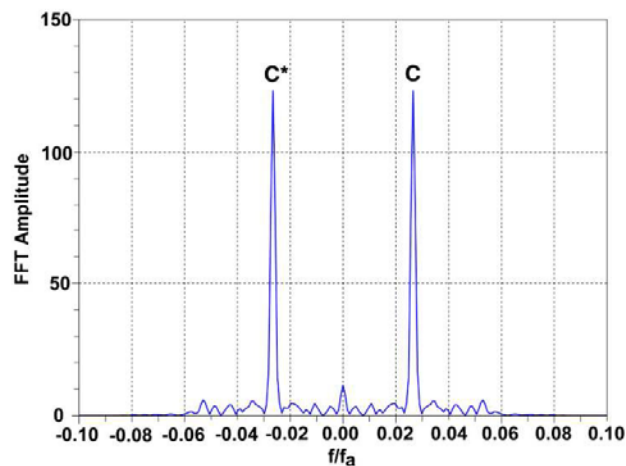


Fig. 14. FFT of an example column of a typical Doppler image

In the next step the sideband C is left shifted on the frequency axis by f_0 to get the spectrum C containing the phase difference information in the base band (demodulation). To obtain the distribution of the phase difference $\Delta\varphi(x, y)$ the spectrum is transformed back from frequency domain $C(x, y)$ to the image domain $c(x, y)$ using the Inverse Fast Fourier Transformation (IFFT). Finally the complex logarithm of $c(x, y)$ is calculated as follows:

$$\ln[c(x, y)] = \ln\left[\frac{1}{2}b(x, y)\right] + j\Delta\varphi(x, y). \quad (16)$$

The phase difference $\Delta\varphi(x, y)$ is now completely separated from any amplitude variation in the imaginary part of equation (16). Applying the operations described pixel by pixel to all image columns of the reference and Doppler pictures, the change of the phase differences between both is as:

$$d(\Delta\varphi)(x, y) = \Delta\varphi_D(x, y) - \Delta\varphi_R(x, y). \quad (17)$$

The phase difference variations are proportional to the velocity variation dv :

$$dv(x, y) = v(x, y) = \frac{A}{2\pi} d(\Delta\varphi)(x, y). \quad (18)$$

The value of the proportionality factor A in equation (18) depends on the length of the glass block used in the MI and the wavelength of the laser used. With the reference image being defined as zero velocity the absolute velocity $v(x, y)$ is equal to the velocity variation $dv(x, y)$, see equation (18).

6.4 Error estimations

To verify the accuracy of the FFT-based method, the measurement error between the DPV velocity profile of the sphere flow (Fig. 16) and a numerical CFD++ simulation done by Havermann, 2007 at the same flow conditions has been considered. The absolute velocity difference between the DPV and CFD++ data in relation to the maximum velocity shift allowed by the MI setup (about 2128 m/s for the sphere flow experiment) gives an estimation of the absolute error of the DPV experiments performed. It came out that there is a deviation possible of about 2.5% of the maximum range, close to 50 m/s, i.e. ± 25 m/s. This error may be explained on the one hand by general measurement uncertainties due to noise (see section 4.1). Nevertheless, there are also comparably high errors in the image areas containing the bow wave and solid surfaces (close to the flow) that may not easily

be explained by measurement uncertainties: These influences are examined and tested by Pichler, and George, 2007 in detail.

6.5 FFT velocity results

6.5.1 Wedge flow

The velocity picture in Fig. 15 shows in pseudo colors the vertical velocity component v present in both the free stream flow and behind the oblique attached shock wave placed in front of the wedge. On the wedge, the measured velocity is of the order of $v \approx 550 \pm 25$ m/s, as visualized in orange/red in the velocity picture, being constant between bow wave and wedge surface.

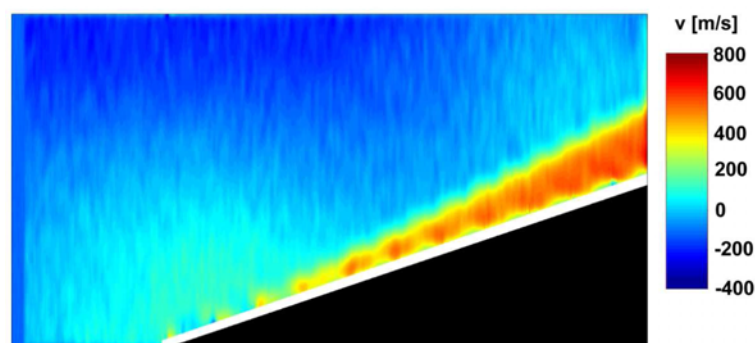


Fig. 15. FFT processed velocity distribution over the wedge

6.5.2 Sphere flow

The vertical velocity distribution for a sphere is represented in Figure 16. Over the sphere, the flow

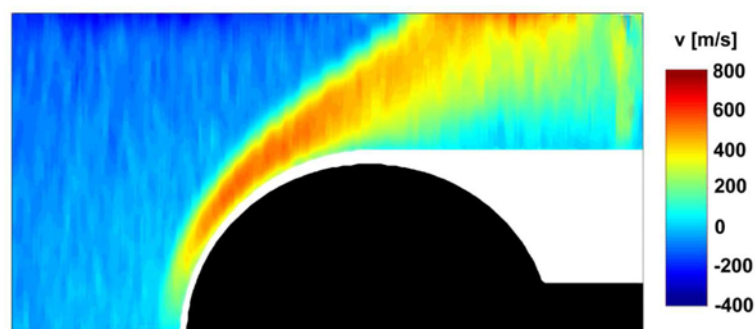


Fig. 16. FFT processed velocity distribution around a sphere

accelerates to slightly more than 500 ± 25 m/s. The results of the sphere as well as the wedge velocity measurements are, regarding an error of about ± 25 m/s (Chapter 6.4), in good agreement with PIV measurements done by Havermann et al., 2002 and with numerical estimations (Havermann, 2007).

7. Conclusions

Newly developed DPV picture processing algorithms have been developed and applied to overcome some disadvantages of the procedures used in the past, such as formerly necessary user manipulations that are now no more required. Two different techniques, LES (Recursive Least

Squares Estimators) and a FFT-based algorithm (Fast Fourier Transformations) have been developed to analyze the DPV Doppler pictures automatically without user interaction for velocity determination in a light sheet crossing a gas flow. They were tested by taking DPV pictures of well-known wedge and sphere flows. At the moment the FFT processing scheme is able to better process the velocity jump across the bow wave compared to LES (Least Squares Estimators).

References

- Havermann, M., CFD++ calculation of the vertical velocity component around a sphere model in a hypersonic flow, ISL internal notice, (2007)
- Havermann, M., Haertig, J., Rey, C., George, A., Application of particle image velocimetry to high-speed supersonic flows in a shock tunnel, Proceedings of the 11th International Symposium on Applications of Laser Techniques to Fluid Mechanics (Lisbon), (2002)
- Merzkirch, W., Laser-Speckle-Velocimetrie, „Lasermethoden in der Strömungsmechanik“, Editor B. Ruck BAT-Fachverlag, Stuttgart, (1990)
- Meyers, J. F., Doppler Global Velocimetry the next generation, AIAA 92-3897, (1992)
- Oertel, H., Seiler, F., George, A., Visualisierung von Geschwindigkeitsfeldern mit Dopplerbildern, (Visualization of velocity fields with Doppler pictures), ISL-Report R 115/82, (1982)
- Pfaff, R., George, A., Seiler, F., Srulijes, J., Dopplerbild-Verfahren-Entwicklung einer neuen Auswertemethode, ISL-Report R 124/2005, (2005)
- Pfaff, R., Automated processing of the ISL Doppler images, Bachelor thesis, Fern Universität Hagen, (2007)
- Pfaff, R., Pichler, A., George, A., Seiler, F., Model based image processing for flow visualisation, Proceedings of the International Conference on Systems Science (Wroclaw, Poland), (2007)
- Pichler, A., George, A., Seiler, F., Srulijes, J., Havermann, M., Doppler Picture Velocimetry (DPV) applied to hypersonics, Proceedings of the 26th International Symposium on Shock Waves (Göttingen, Germany), (2007)
- Pichler, A., George, A., Das Dopplerbild-Verfahren (DPV), Automatische Auswertung nach der FFT-Methode, ISL-Report R-109/2007, (2007)
- Seiler, F., Srulijes, J., George, A., A Doppler-picture camera for velocity field visualization, Proceedings of the 12th International Congress on Instrumentation in Aerospace Simulation Facilities (Williamsburg, USA), (1987)
- Seiler, F., George, A., Leopold, F., Havermann, M., Srulijes, J., Enhanced Doppler Picture Velocimetry (DPV) for planar velocity measurements in high speed shock tunnel flow, Proceedings of the 10th International Symposium on Flow Visualization (Kyoto, Japan), (2002)
- Seiler, F., George, A., Havermann, M., Srulijes, J., Doppler Picture Velocimetry (DPV) applied to high-speed shock tunnel flows, Proceedings of the 11th Int. Symposium on Flow Visualization (Notre Dame, Indiana, USA), (2004)
- Seiler, F., George, A., Srulijes, J., Havermann, M., Progress in Doppler Picture Velocimetry (DPV) Technique, Proceedings of the 12th International Symposium on Flow Visualization (Göttingen, Germany), (2006)
- The MathWorks Inc., Image Processing, www.mathworks.com/applications/image_processing/description/analysis.html, (2005)